Journal of Colloid and Interface Science 655 (2024) 748–759

Contents lists available at ScienceDirect

Journal of Colloid And Interface Science

journal homepage: www.elsevier.com/locate/jcis

Boosting the sodium storage performance of iron selenides by a synergetic effect of vacancy engineering and spatial confinement

Peng Wang [a], Yuxiang Chen [a], Xiangyue Liao [a], Qiaoji Zheng [a], Ruyi Zhao [b,*], Kwok-Ho Lam [c,*], Dunmin Lin [a,*]

[a] College of Chemistry and Materials Science, Sichuan Normal University, Chengdu 610066, China
[b] School of Energy Science and Engineering, Harbin Institute of Technology, Harbin 150001, China
[c] Centre for Medical and Industrial Ultrasonics, James Watt School of Engineering, University of Glasgow, Glasgow, Scotland, UK

HIGHLIGHTS

- Se vacancies adjust the electron density and improve the conductivity of material.
- Se vacancies promote Na^+ migration and enhance the reaction kinetics of material.
- The carbon confinement strengthens the structural stability of the electrode.
- The material possesses excellent electrochemical properties.

GRAPHICAL ABSTRACT

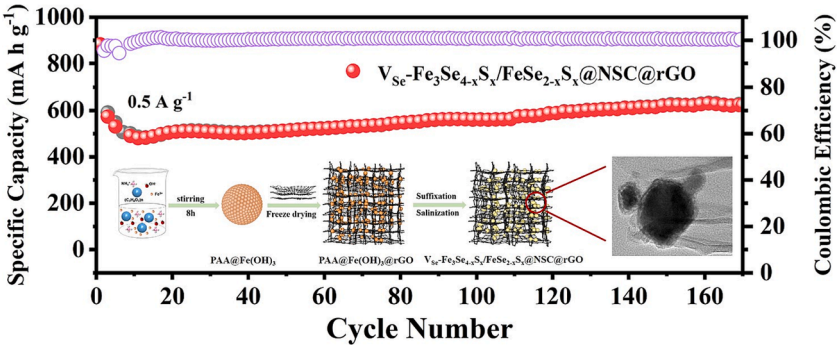

ARTICLE INFO

Keywords:
Sodium-ion batteries
Anode materials
Iron selenide
S-doping
Electron density
Se vacancy
Carbon confinement

ABSTRACT

Recently, iron selenides have been considered as one of the most promising candidates for the anodes of sodium-ion batteries (SIBs) due to their cost-effectiveness and high theoretical capacity; however, their practical application is limited by poor conductivity, large volume variation and slow reaction kinetics during electrochemical reactions. In this work, spatially dual-carbon-confined V_{Se}-$Fe_3Se_{4-x}S_x$/$FeSe_{2-x}S_x$ nanohybrids with abundant Se vacancies (V_{Se}-$Fe_3Se_{4-x}S_x$/$FeSe_{2-x}S_x$@NSC@rGO) are constructed via anion doping and carbon confinement engineering. The three-dimensional crosslinked carbon network composed of the nitrogen-doped carbon support derived from polyacrylic acid (PAA) and reduced graphene enhances the electronic conductivity, provides abundant channels for ion/electron transfer, ensures the structure integrity, and alleviates the agglomeration, pulverization and volume change of active material during the chemical reactions. Moreover, the introduction of S into iron selenides induces a large number of Se vacancies and regulates the electron density around iron atoms, synergistically improving the conductivity of the material and reducing the Na^+ diffusion barrier. Based on the aforementioned features, the as-synthesized V_{Se}-$Fe_3Se_{4-x}S_x$/$FeSe_{2-x}S_x$@NSC@rGO electrode possesses excellent electrochemical properties, exhibiting the satisfactory specific capacity of 630.1 mA h g^{-1} after 160 cycles at 0.5 A/g and the reversible capacity of 319.8 mA h g^{-1} after 500 cycles at 3 A/g with the low-

* Corresponding authors.
E-mail addresses: 20S102159@stu.hit.edu.cn (R. Zhao), kwokho.lam@glasgow.ac.uk (K.-H. Lam), ddmd222@sicnu.edu.cn (D. Lin).

https://doi.org/10.1016/j.jcis.2023.11.074
Received 20 August 2023; Received in revised form 6 November 2023; Accepted 11 November 2023
Available online 13 November 2023

capacity attenuation of 0.016 % per cycle. This investigation provides a feasible approach to develop high-performance anodes for SIBs via a synergetic strategy of vacancy engineering and carbon confinement.

1. Introduction

In recent years, lithium-ion batteries (LIBs) have been widely used in electronic devices and electric vehicles because of their high energy density, long service life and portability [1–3]. Nevertheless, due to the extreme shortage and geographically uneven distribution of lithium resources, the cost of LIBs is much higher than that of other energy storage devices [4]. Thus, it is vital to seek alternative energy storage devices to replace LIBs. In the past few years, sodium-ion batteries (SIBs) have attracted much attention due to their abundant sodium resources and similar working principle to LIBs [5–7]. Unfortunately, compared with Li^+ (0.76 Å, and M = 7), Na^+ (0.95 Å, and M = 23) possesses much larger ionic radius and higher relative molecular mass, resulting in the slow reaction kinetics and severe volume change of the electrode material during Na^+ de/insertion [8,9].

To address the aforementioned issues, numerous anodes for SIBs have been extensively investigated, including carbon-based materials, alloy materials and conversion-type materials [10–14]. Among various candidates for the anodes of SIBs, the conversion-type iron selenide materials have been particularly favored because of their high theoretical capacity, abundant resources and low cost [15–17]. However, the sluggish kinetics and large volumetric change during the de/insertion of Na^+ ions have been the major hindrance [18]. Recently, structural optimization, carbon confinement, and doping have been widely used to enhance the reaction kinetics of iron selenides and alleviate the volume change during electrochemical reactions [19–22]. For instance, Feng et al. designed porous yolk shell-structured $FeSe_2$@NDC nanocubes, alleviating the severe volumetric change of iron selenide [23] and thus providing excellent cycle stability (403.3 mA h g^{-1} at 5 A/g after 2000 cycles); Liu et al. embedded the heterogeneous Fe_3Se_4/FeSe nanoparticles into the carbon nanofiber by a electrospinning method, which constrained the volume change of the active material and thus improved the cycle life (417.4 mA h g^{-1} at 0.5 A/g after 200 cycles) [24]; and Kong et al. synthesized Ni-doped $FeSe_2$/Fe_3Se_4 heterojunction materials by hydrothermal and selenization treatments [25], where Ni doping enlarges the lattice spacing of iron selenide and reduces the diffusion nowel of Na^+, while rich heterojunction surface enhances the conductivity and stability of the material, providing the capacity of 352.9 mA h g^{-1} at 0.5 A/g after 500 cycles. However, among the strategies to improve the performance of iron selenides, the construction of vacancies to improve the sodium storage performance of iron selenides is rarely seen. On the other hand, it has been known that anion vacancies play a pivotal role in enhancing the electrochemical properties of electrodes. Many studies have shown that anionic vacancies could excite a large number of high-energy unsaturated active sites, which act as defect centers and induce electrons around metal atoms, making the band gap smaller and improving the conductivity of the material [26,27]. For example, Yao et al. introduced Si into MIL-125 metal–organic framework and obtained SiO_2/TiO_{2-x}@C nanosheets after annealing under Ar atmosphere [28], where abundant oxygen vacancies narrow the band and reduce the Na^+ diffusion barrier of the material, enhancing the sodium storage performance of TiO_2 (190 mA h g^{-1} at 2 A/g after 2500 cycles); Ma et al. prepared ultrathin MoS_2/C nanosheets with abundant S vacancies by a chemical reduction method [29], where S vacancies expose rich active sites and promote Na^+ insertion, showing excellent sodium storage performance (473 mA h g^{-1} at 1 A/g after 100 cycles). It has been noted that the electronegativity of S (2.58) is higher than that of Se (2.48) and thus it may be expected that the introduction of S into iron selenides may cause electrons around Fe^{2+} to be captured by S, resulting in the oxidation of part of Fe^{2+} to Fe^{3+} to generate selenium vacancies and the regulation of electron structure around Fe atoms, which are beneficial to reducing the diffusion carrier of Na^+, exposing more active sites and enhancing the conductively of the materials.

Herein, spatially dual-confined V_{Se}-$Fe_3Se_{4-x}S_x$/$FeSe_{2-x}S_x$ nanohybrids with abundant Se vacancies (V_{Se}-$Fe_3Se_{4-x}S_x$/$FeSe_{2-x}S_x$@NSC@rGO) are successfully synthesized via the comprehensive strategy of anion doping and carbon confinement engineering by the combined processes of freeze-drying treatment and sulfurization/selenization using PAA@$Fe(OH)_3$@rGO as the precursor. The spatially dual-carbon confinement improves the electronic conductivity, ensures the structure integrity and inhibits the agglomeration, pulverization and volume change of active material during electrochemical reactions [30,31]. Simultaneously, the introduction of S induces a of Se vacancies and regulates the electron density around Fe atoms, improving the conductivity of the material and fastening Na^+ ions de/insertion kinetics [29,32]. Consequently, the V_{Se}-$Fe_3Se_{4-x}S_x$/$FeSe_{2-x}S_x$@NSC@rGO exhibits excellent reversible capacity of 630.1 mA h g^{-1} after 160 cycles at 0.5 A/g and satisfactory cycle performance of 319.8 mA h g^{-1} at 3 A/g after 500 cycles.

2. Experimental section

2.1. Materials

Poly(acrylic acid) solution with 50 % (MW ~ 3000) was acquired fromAladdin Chemical Co., Ltd., ammonia solution (NH_3, AR) and sulfur powder (S, AR) were purchased from Cologne Chemical Co., Ltd., iron nitrate nonahydrate ($Fe(NO_3)\cdot 9H_2O$, AR) and selenium powder (Se, CP) were obtained from Sinopharm Chemical Reagent Co., Ltd., and graphene oxide was purchased from XFNANO Co., Ltd., 2-propanol (AR) was acquired from Shanghai Titan Technology Co., Ltd. None of the above chemicals were further purified.

2.2. Synthesis of V_{Se}-$Fe_3Se_{4-x}S_x$/$FeSe_{2-x}S_x$@NSC@rGO

Synthesis of PAA@$Fe(OH)_3$ nanoparticles: 1 ml ammonia solution and 0.5 ml Poly (acrylic acid) 50 % solution (MW ~ 3000) were added to a 500 ml beaker. Then 50 ml deionized water was added to the beaker and stirred for 40 mins. 300 ml 2-propanol was further added to the above solution, quickly turning into a white suspension. Then, 0.5 g Fe $(NO_3)\cdot 9H_2O$ was slowly added to the white suspension and stirred continuously at room temperature for 8 h. At last, the brown product was washed with 2-propanol several times to obtain PAA@$Fe(OH)_3$ nanoparticles.

Synthesis of PAA@$Fe(OH)_3$ @rGO: 30 mg of rGO was dispersed into 30 ml of deionized water with ultrasonication for 10 h as solution A. In the meantime, PAA@$Fe(OH)_3$ was mixed with 30 ml of 2-propanol to form solution B. Subsequently, solution A was slowly added to solution B by drip and ultrasonication was performed for 2 h as solution C. Finally, the solution C was freeze-dried for 48 h to obtain PAA@$Fe(OH)_3$@rGO.

Synthesis of V_{Se}-$Fe_3Se_{4-x}S_x$/$FeSe_{2-x}S_x$@NSC@rGO: The obtained PAA@$Fe(OH)_3$@rGO (100 mg) with 50 mg S and 200 mg Se were put into an alumina boat separately. The annealing treatment was carried out in N_2 atmosphere at 450 ℃ for 2 h with a ramp of 2 ℃ min^{-1}. After natural cooling, the V_{Se}-$Fe_3Se_{4-x}S_x$/$FeSe_{2-x}S_x$@NSC@rGO was obtained.

2.3. Synthesis of Fe_7S_8@NSC@rGO and Fe_3Se_4/$FeSe_2$@NC@rGO

The obtained PAA@$Fe(OH)_3$@rGO (100 mg) with 200 mg S were put into an alumina boat separately. The annealing treatment was carried out in N_2 atmosphere at 450 ℃ for 2 h with a ramp of 2 ℃ min^{-1}. After natural cooling, the Fe_7S_8@NSC@rGO was obtained.

The synthesis method of $Fe_3Se_4/FeSe_2$@NC@rGO is similar as above, only 200 mg S is replaced by 200 mg Se.

2.4. Materials characterization

The phase structure of the synthetic material was characterized by X-ray powder diffraction (XRD, Smart Lab, Rigaku with Cu Kα radiation). The Raman spectrum was measured by Raman spectrometer (Renishaw RM2000, UK, with a 514 nm laser wavelength operated at a power of 5 mW). The field emission scanning electron microscopy (FEI/quanta250) and field emission transmission electron microscopy (FE-TEM, G2F20, USA) were used to observe the morphological characteristics and microstructure of materials. The chemical bonds between elements the material were characterized by X-ray photoelectron spectroscopy (XPS, PHI 5000). A field emission transmission electron microscope (Zeiss/sigma 500) with an energy dispersive spectroscopy detector was used to test energy-dispersive spectrum (EDS). The pore properties and specific surface area of the sample were obtained by the multipoint Brunauer-Emmett-Teller (BET, ASAP2020HD8 Surface Area and Porosity Analyzer) based on the N_2 adsorption–desorption isotherms principle. The vacancies of the material were characterized by electron paramagnetics (EPR, Bruck-E500). The element content was measured by inductively coupled plasma emission spectrometry (ICP-OES, Agilent 5110).

2.5. Electrochemical measurements

The anode electrode was prepared by mixing active substances including acetylene black (Super P) and polyvinylidene fluoride (PVDF) in *N*-methypyrrolidone (NMP) at a mass ratio of 7:2:1, specifically. The loading mass of the electrodes we prepared was all about 1.5 mg, and the mass of the active substance from the composition ratio of the above electrode to be about 1.05 mg. A coin-operated (CR2032) battery was assembled in an argon-filled glove box using sodium metal as the counter electrode, copper foil as the collector, glass fiber membrane as the separator, and 1 M NaF_3SO_3 dissolved in diethylene glycol dimethyl ether (DEGDME) as the electrolyte. All the galvanostatic cycle tests were performed on a multichannel battery tester (LAND, CT2100A, China) with the voltage window of 0.1 V – 3.0 V at room temperature. The electrochemical impedance spectroscopy (EIS) and cyclic voltammetry (CV) were tested on the electrochemical workstation (CHI 660E, Shanghai, China). The sodium ion full battery was assembled using V_{Se}-$Fe_3Se_{4-x}S_x/FeSe_{2-x}S_x$@NSC@rGO as the anode material, $Na_3V_2(PO4)_3$ as the positive electrode material, and $NaPF_6$ non-aqueous solution (NP-005) as the electrolyte with a voltage window of 1.8 V-3.6 V. The mass ratio of the anode (V_{Se}-$Fe_3Se_{4-x}S_x/FeSe_{2-x}S_x$@NSC@rGO) and the cathode ($(Na_3V_2(PO_4)_3$) is about 1: 4. In addition, the specific capacity of the full cell was calculated based on the mass of the anode (V_{Se}-$Fe_3Se_{4-x}S_x$/$FeSe_{2-x}S_x$@NSC@rGO).

2.6. Theoretical calculation

Firstly, the supercell models of intrinsic $FeSe_2$, $FeSe_{2-x}S_x$, Fe_3Se_4 and $Fe_3Se_{4-x}S_x$ were constructed based on Materials Studio software, and then imported into Gaussian09 software for model optimization. Finally, the Density of States (DOS) map was drawn using Multiwfn software. Its electronic structure was calculated and investigated. Gaussian09 software was used to optimize the material model. The non-local exchange correlation functional (PBE) under generalized gradient approximation (GGA) was used in the simulation calculation process, and the interaction between ion real and valence electrons was performed by projection affixed plane wave (PAW) method. To avoid interactions between the plates, the vacuum layer was set to 12 Å to fix the bottom layer atoms and leave the remaining two layers atoms in a relaxation state. The grid size of the Brillouin zone integral K is $4 \times 4 \times 1$, the cutoff energy is 400 eV, and the energy convergence criterion is set to 10^{-6} eV. The optimized model is loaded into the Multiwfn software and the data is proposed, then the electronic DOS data is processed, and finally the data is imported into the Origin software to draw a complete DOS map.

3. Results and discussion

Fig. 1 shows the preparation process of the V_{Se}-$Fe_3Se_{4-x}S_x/FeSe_{2-x}S_x$@NSC@rGO. Polyacrylic acid (PAA) nanospheres are used as a template. Firstly, $Fe(OH)_3$ is deposited on the surface of the PAA by a precipitation reaction to form PAA@$Fe(OH)_3$ nanospheres with a diameter of ~ 100 nm. Then, rGO aqueous solution is mixed with the PAA@$Fe(OH)_3$ in isopropyl alcohol solution, subjected to ultrasound for 2 h, and freeze-dried for 48 h to obtain PAA@$Fe(OH)_3$@rGO. Finally, the V_{Se}-$Fe_3Se_{4-x}S_x/FeSe_{2-x}S_x$@NSC@rGO is obtained by sulfurization/selenization processes. Due to the higher electronegativity of S than Se, electrons around Fe^{2+} are captured by S during sulfurization/selenization reactions, which induces a large number of Se vacancies and thus regulating the electron density around Fe atoms [33,34].

Fig. 2 and S1 show the morphology and microstructure of the PAA@$Fe(OH)_3$, PAA@$Fe(OH)_3$@rGO, $Fe_3Se_4/FeSe_2$@NC@rGO, Fe_7S_8@NSC@rGO, and V_{Se}-$Fe_3Se_{4-x}Sx/FeSe_{2-x}S_x$@NSC@rGO by scanning electron microscopy (SEM) and transmission electron microscopy (TEM) test. The PAA@$Fe(OH)_3$ precursor exhibits severe agglomeration in Fig. S1a, while the PAA@$Fe(OH)_3$ nanospheres are uniformly anchored on the surface of the rGO as shown in Fig. S1b. Similarly, the $Fe_3Se_4/FeSe_2$@NC@rGO and V_{Se}-$Fe_3Se_{4-x}S_x/FeSe_{2-x}S_x$@NSC are uniformly anchored on the surface of the rGO (Fig. 2a and S1c). However, the Fe_7S_8@NSC@rGO exhibits slight agglomeration (Fig. S1d). In Fig. 2b, a large number of nanospheres are uniformly encapsulated into the rGO. Fig. 2c clearly demonstrates the confinement of carbon nanosphere-containing particles by the rGO, visually exhibiting the structural advantage of the double carbon confinement structure in alleviating the agglomeration of active substances during cycling [35–37]. The high resolution transmission electron microscopy (HR-TEM) image in Fig. 2d shows that the V_{Se}-$Fe_3Se_{4-x}S_x/FeSe_{2-x}S_x$ is encapsulated by the PAA-derived carbon materials and rGO, showing the structural characteristics of double carbon confinement [38]. As shown in Fig. 2d, the lattice fringes with the lattice spacings of 0.245 nm, 0.207 nm and 0.274 nm correspond to (0 1 2) crystal plane of $FeSe_2$, (−1 1 4) and (−2 0 2) crystal planes of Fe_3Se_4, respectively. In addition, the HR-TEM images and corresponding Inverse Fast Fourier transform (IFFT) images reveal a large number of vacancy sites and lattice spacing contraction (dotted lines and circles in red indicate the location in Fig. 2d) [39]. Fig. 2e shows the elemental mappings of the V_{Se}-$Fe_3Se_{4-x}S_x/FeSe_{2-x}S_x$@NSC@rGO. It can be seen that Fe (green), Se (purple), S (orange), C (yellow) and N (blue) elements are uniformly distributed in the material.

Fig. 3a and S2 show the X-ray diffraction (XRD) patterns of the V_{Se}-$Fe_3Se_{4-x}S_x/FeSe_{2-x}S_x$@NSC@rGO, $Fe_3Se_4/FeSe_2$@NC@rGO and Fe_7S_8@NSC@rGO. Clearly, it can be seen that the diffraction peaks of the $Fe_3Se_4/FeSe_2$@NC@rGO are completely consistent with those of $FeSe_2$ (JCPDS No. 004-4751) and Fe_3Se_4 (JCPDS No. 001-5043), indicating that the Fe_3Se_4 and $FeSe_2$ have been successfully synthesized. After the introduction of S, the diffraction peaks of the V_{Se}-$Fe_3Se_{4-x}S_x/FeSe_{2-x}S_x$@NSC@rGO is slightly shifted towards low angles, which is due to the fact that S is smaller than Se, causing the lattice shrinkage. In addition, the diffraction peak intensities of the V_{Se}-$Fe_3Se_{4-x}S_x/FeSe_{2-x}S_x$@NSC@rGO become weaker compared to those of the $Fe_3Se_4/FeSe_2$@NC@rGO, which is attributed to a large number of Se vacancies induced by the introduction of S [40]. In Fig. S2, the diffraction peaks of Fe_7S_8@NSC@rGO can be well indexed to those of Fe_7S_8 (JCPDS No. 25-0411). In order to further prove the existence and valence distribution of each element in the material, X-ray photoelectron spectroscopy (XPS) is examined on the material. Fig. S3a shows that Fe, Se, S, N and C elements exist in the V_{Se}-$Fe_3Se_{4-x}S_x/FeSe_{2-x}S_x$@NSC@rGO, while Fig. 3b shows that the Fe $2p_{3/2}$ double peaks of V_{Se}-$Fe_3Se_{4-x}S_x/FeSe_{2-}$

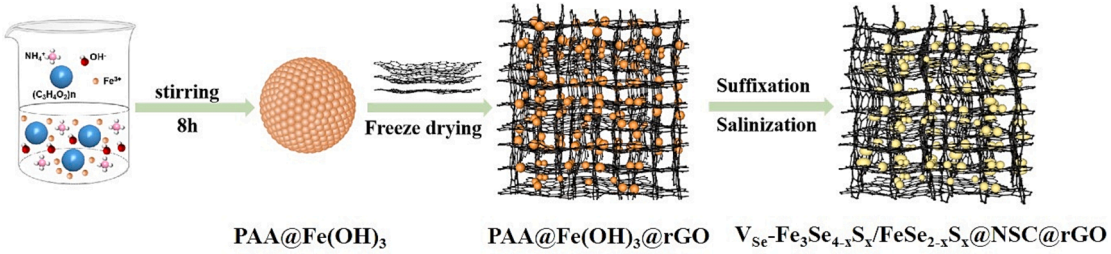

Fig. 1. Synthesis process of V_{Se}-$Fe_3Se_{4-x}S_x$/$FeSe_{2-x}S_x$@NSC@rGO.

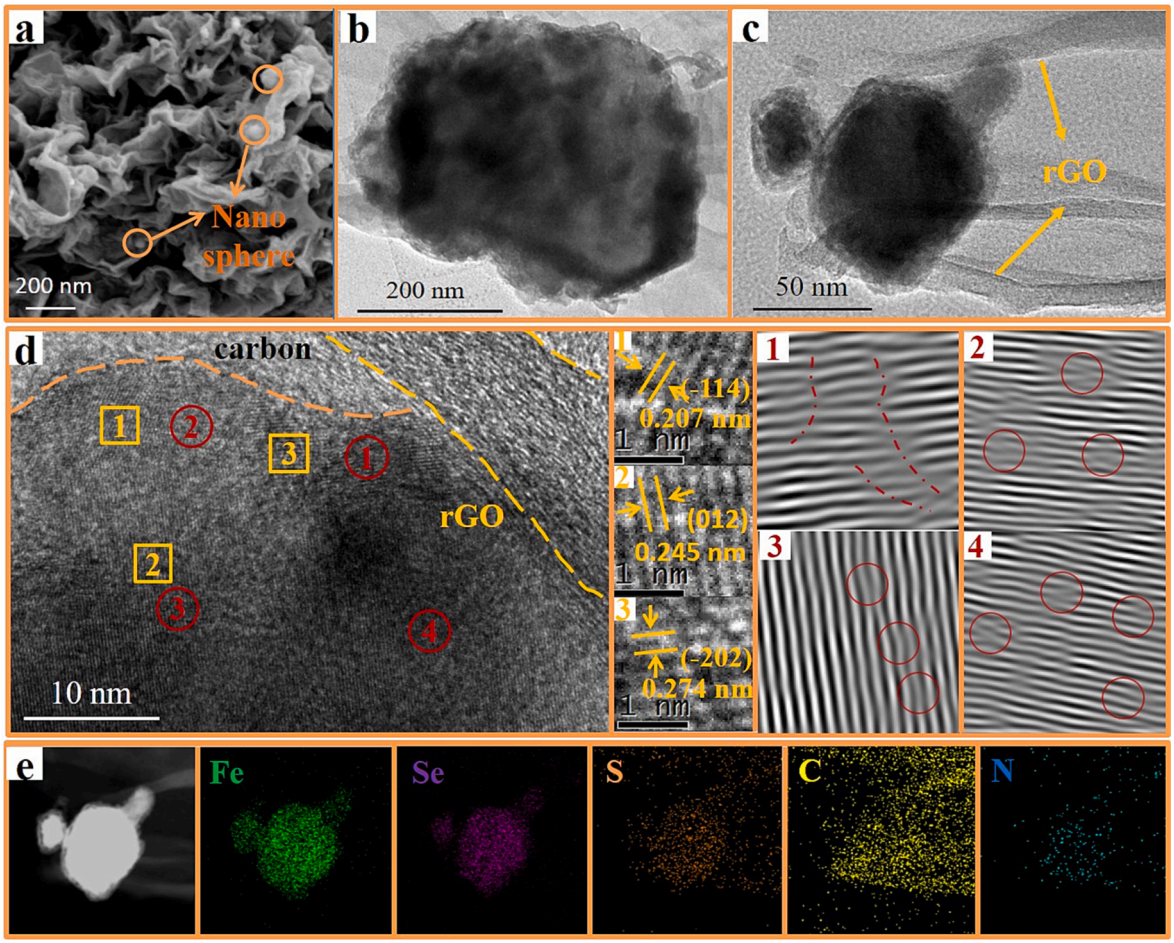

Fig. 2. (a) SEM image of V_{Se}-$Fe_3Se_{4-x}S_x$/$FeSe_{2-x}S_x$@NSC@rGO; (b-c) TEM images of V_{Se}-$Fe_3Se_{4-x}S_x$/$FeSe_{2-x}S_x$@NSC@rGO; (d) HRTEM images of V_{Se}-$Fe_3Se_{4-x}S_x$/$FeSe_{2-x}S_x$@NSC@rGO; (e) TEM EDS elemental images of V_{Se}-$Fe_3Se_{4-x}S_x$/$FeSe_{2-x}S_x$@NSC@rGO.

$_xS_x$@NSC@rGO are located at 710.9 eV and 724.3 eV, respectively. It is worth noting that there is a negative shift (0.3 eV) for the V_{Se}-$Fe_3Se_{4-x}S_x$/$FeSe_{2-x}S_x$@NSC@rGO compared with the twin peaks of the Fe $2p_{3/2}$ (711.2 eV and 724.6 eV) of the Fe_3Se_4/$FeSe_2$@NC@rGO. The negative shift of Fe^{3+} peak indicates that the interaction between Fe and Se atoms is weakened, which is caused by the joint attraction of Se vacancies and S atoms to the surrounding electrons of Fe atoms [34]. On the contrary, the two Fe $2p_{1/2}$ peaks of the V_{Se}-$Fe_3Se_{4-x}S_x$/$FeSe_{2-x}S_x$@NSC@rGO show a positive deviation (0.2 eV) from those of the Fe_3Se_4/$FeSe_2$@NC@rGO [40]. As shown in Fig. S5, the peaks of the Fe$2p_{3/2}$ and Fe$2p_{1/2}$ of the Fe_7S_8@NSC@rGO are 711.3 eV, 724.7 eV, 712.8 eV and 727.2 eV, respectively [16]. Fig. 3c shows the Se 3d spectra of the V_{Se}-$Fe_3Se_{4-x}S_x$/$FeSe_{2-x}S_x$@NSC@rGO and Fe_3Se_4/$FeSe_2$@NC@rGO. Compared with the peaks of Se $3d_{5/2}$ (55.3 eV) and Se $3d_{3/2}$ (56.3 eV) of the Fe_3Se_4/FeSe$_2$@NC@rGO, the positive displacements (0.2 eV) for the Se $3d_{5/2}$ (55.5 eV) and Se $3d_{3/2}$ (56.5 eV) peaks of the V_{Se}-$Fe_3Se_{4-x}S_x$/$FeSe_{2-x}S_x$@NSC@rGO are due to internal vacancies [39,41]. The Se $3d_{3/2}$ and Se$3d_{5/2}$ in the materials indicate Se vacancy and lattice selenium, respectively. Obviously, the area ratio of Se $3d_{3/2}$ to Se$3d_{5/2}$ in the V_{Se}-$Fe_3Se_{4-x}S_x$/$FeSe_{2-x}S_x$@NSC@rGO (36.91 %) is higher than that of the Fe_3Se_4/$FeSe_2$@NC@rGO (29.73 %), indicating the increased Se vacancies induced by the introduction of S [41,42]. Fig. 3d shows the XPS peaks of the S-Se (160.9 eV), S^{2-} (162.2 eV and 164.2 eV) and C—S (165.3 eV) in the V_{Se}-$Fe_3Se_{4-x}S_x$/$FeSe_{2-x}S_x$@NSC@rGO, proving the successful introduction of S into the iron selenides and carbon layers [34]. In addition, it can be seen from Fig. S5b that the peaks of the $S2p^{3/2}$ and $S2p^{1/2}$ of the Fe_7S_8@NSC@rGO are 161.6 eV, 163.8 eV and 162.5 eV, 165.3 eV, respectively. As shown in Fig. 3e, the XPS peaks of N1s (398.5 eV, 400.1 eV and 401.7 eV) for the V_{Se}-$Fe_3Se_{4-x}S_x$/$FeSe_{2-x}S_x$@NSC@rGO represent pyridine nitrogen, pyrrole nitrogen, and

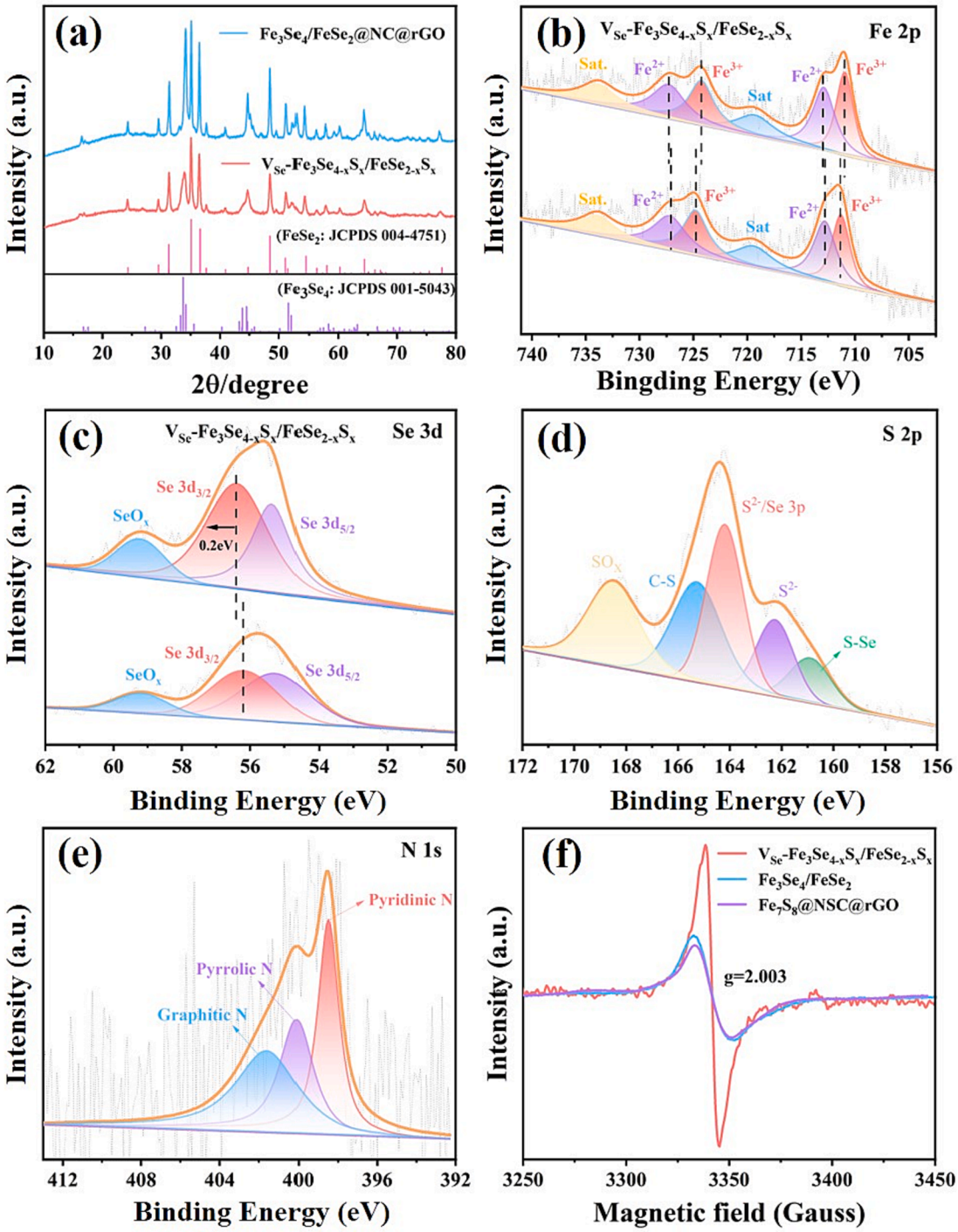

Fig. 3. (a) XRD patterns of V_{Se}-$Fe_3Se_{4-x}S_x$/$FeSe_{2-x}S_x$@NSC@rGO and Fe_3Se_4/$FeSe_2$@NC@rGO; (b) XPS spectra of Fe 2p in V_{Se}-$Fe_3Se_{4-x}S_x$/$FeSe_{2-x}S_x$@NSC@rGO and Fe_3Se_4/$FeSe_2$@NC@rGO; (c) XPS spectra of Se 3d in V_{Se}-$Fe_3Se_{4-x}S_x$/$FeSe_{2-x}S_x$@NSC@rGO and Fe_3Se_4/$FeSe_2$@NC@rGO; (d) XPS spectra of S 2p in V_{Se}-$Fe_3Se_{4-x}S_x$/$FeSe_{2-x}S_x$@NSC@rGO; (e) XPS spectra of N 1s in V_{Se}-$Fe_3Se_{4-x}S_x$/$FeSe_{2-x}S_x$@NSC@rGO; (f) EPR spectra of V_{Se}-$Fe_3Se_{4-x}S_x$/$FeSe_{2-x}S_x$@NSC@rGO, Fe_3Se_4/$FeSe_2$@NC@rGO and Fe_7S_8@NSC@rGO.

graphene nitrogen, respectively, similar the Fe_3Se_4/$FeSe_2$@NC@rGO (Fig. S4a) and Fe_7S_8@NSC@rGO (Fig. S5c). Moreover, form the XPS spectrum of C1s (Fig. S3b) for the V_{Se}-$Fe_3Se_{4-x}S_x$/$FeSe_{2-x}S_x$@NSC@rGO, a C—N peak can be observed at 285.1 eV, showing the presence of the doping of N into carbon [37], similar to the Fe_3Se_4/$FeSe_2$@NC@rGO (Fig. S4b) and Fe_7S_8@NSC@rGO (Fig. S5d). In order to further confirm the existence of Se vacancies, electron paramagnetic resonance (EPR) test is performed on the V_{Se}-$Fe_3Se_{4-x}S_x$/$FeSe_{2-x}S_x$@NSC@rGO, Fe_3Se_4/$FeSe_2$@NC@rGO and Fe_7S_8@NSC@rGO. Clearly, the V_{Se}-$Fe_3Se_{4-x}S_x$/$FeSe_{2-x}S_x$@NSC@rGO exhibits the strongest EPR signal at g = 2.003 (Fig. 3f) among the three materials, suggesting the existence of a number of Se vacancies [43,44].

To further study the chemical forms of carbon in the composites, Fig. 4a shows two main peaks (~1355 and ~ 1580 cm^{-1}) in the Raman Atlas, in which one belongs to sp^3-hybrid disorder (D) and the other to sp^2-hybrid graphene (G). According to the I_D/I_G values of the three samples in the Raman spectra, the defect carbon content of the V_{Se}-$Fe_3Se_{4-x}S_x$/$FeSe_{2-x}S_x$@NSC@rGO is higher than that of the other two

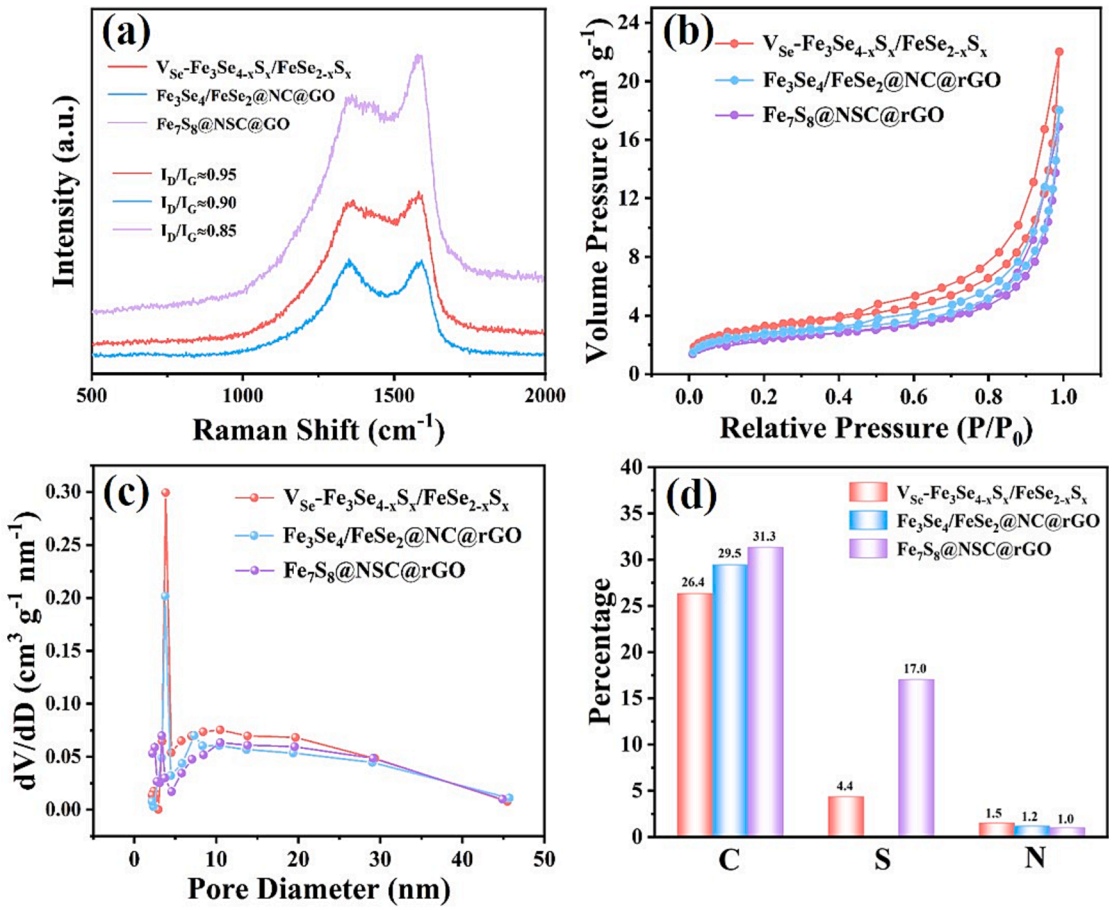

Fig. 4. (a) Raman spectra, (b) N_2 adsorption/desorption isotherms, (c) pore size distributions and (d) CHNS element analysis of V_{Se}-$Fe_3Se_{4-x}S_x$/$FeSe_{2-x}S_x$@NSC@rGO, Fe_3Se_4/$FeSe_2$@NC@rGO and Fe_7S_8@NSC@rGO (the experimental data are obtained from two repeated tests and the experimental error is less than 2 %).

samples [45], which is beneficial to the full immersion of electrolyte in the material, and exposing expose more sodium storage sites. In Brunauer-Emmett-Teller (BET) test (Fig. 4b, c), the V_{Se}-$Fe_3Se_{4-x}S_x$/$FeSe_{2-x}S_x$@NSC@rGO shows a large specific surface area and mesoporous pore size (4– 45 nm). In addition, both specific surface area and pore volume of the V_{Se}-$Fe_3Se_{4-x}S_x$/$FeSe_{2-x}S_x$@NSC@rGO are superior to the other two samples. It can be seen from the CHNS element analysis bar chart (Fig. 4d) that the carbon and nitrogen contents of the V_{Se}-$Fe_3Se_{4-x}S_x$/$FeSe_{2-x}S_x$@NSC@rGO, Fe_3Se_4/$FeSe_2$@NC@rGO and Fe_7S_8@NC@rGO are 26.4 % and 1.51 %, 29.5 % and 1.2 %, 31.3 % and 1.0 %, respectively. The S doping content in the V_{Se}-$Fe_3Se_{4-x}S_x$/$FeSe_{2-x}S_x$@NSC@rGO material is ~ 4.4 wt%, which is similar to the Energy Dispersive Spectroscopy (EDS) test result (Fig. S6).

The electrochemical performance of the V_{Se}-Fe_3Se_{4-x}Sx/$FeSe_{2-x}S_x$@NSC@rGO, Fe_7S_8@NSC@rGO and Fe_3Se_4/$FeSe_2$@NC@rGO is tested in a coin-type 2032 cell. Fig. 5a exhibits that the cyclic voltammetry (CV) curves of the V_{Se}-Fe_3Se_{4-x}Sx/$FeSe_{2-x}S_x$@NC@rGO in the initial three cycles almost coincide at the scan rate of 0.1 mV s^{-1}, indicating strong electrochemical reversibility. It is worth mentioning that two small reduction peaks occur at 1.0 – 1.2 V during the first cathode scan, and disappear in the subsequent cycles [46]. This is attributed to the insertion of Na^+, accompanied by the irreversible decomposition of the electrolyte, to form an interfacial membrane (SEI) with the solid electrolyte [16]. A broad peak at 0.40 V – 0.47 V may be attributed to the conversion reaction of $FeSe_2$ and Fe_3Se_4 components and the production of Fe^0 [46]. During the subsequent anodic scan, the presence of three distinct oxidation peaks at 1.5 V, 1.7 V, and 2.3 V is attributed to remodeling of $FeSe_2$ and Fe_3Se_4. As shown in Fig. 5b, the charging and discharging capacities of the V_{Se}-$Fe_3Se_{4-x}S_x$/$FeSe_{2-x}S_x$@NSC@rGO electrode at 0.5 A/g are 882.2 mA h g^{-1} and 648.4 mA h g^{-1}, respectively, and the initial Coulomb efficiency (CE) is 73.50 %. The relative low CE in the first cycle is due to the irreversible reaction of SEI formed in the discharge process [16]. The CE increases to 96.16 % after the second cycle and then remains stable, while the specific capacity gradually increases in the subsequent cycles. At the ampere density of 0.5 A/g (Fig. 5c), the V_{Se}-$Fe_3Se_{4-x}S_x$/$FeSe_{2-x}S_x$@NSC@rGO electrode delivers a reversible capacity of 630.1 mA h g^{-1} after 160 cycles. It is worth noting that the capacity of the V_{Se}-$Fe_3Se_{4-x}S_x$/$FeSe_{2-x}S_x$@NSC@rGO electrode shows a downward trend after the first cycle, which is because in the early cycle, Na^+ and anions in the electrolyte repeatedly form a solid electrolyte interface (SEI) on the electrode surface, and part of the sodium ions are consumed, resulting in irreversible loss of capacity [47,48]. When SEI is gradually stabilized, the kinetics of Na^+ diffusion is enhanced, and the sodiation-induced reactivation also leads to a gradual increase in capacity [39,49]. In contrast, the specific capacity of the Fe_7S_8@NC@rGO electrode decreases rapidly after 70 cycles and even drops to only 252.6 mA h g^{-1} after 130 cycles. The Fe_3Se_4/$FeSe_2$@NC@rGO electrode inherits the excellent cycling stability of selenides, but the specific capacity is much lower than that of the V_{Se}-$Fe_3Se_{4-x}S_x$/$FeSe_{2-x}S_x$@NSC@rGO (371.2 mA h g^{-1} after 160 cycles). As shown in Tab. S1, the reversible capacity of the $Fe_3Se_{4-x}S_x$/$FeSe_{2-x}S_x$@NSC@rGO is comparable /superior to that of previously reported selenide and sulfide anodes. Fig. 5d shows the rate performance of the three samples at different current densities. When the current densities are 0.1, 0.2, 0.5, 1, 2 and 5 A/g, the average discharge capacities of the V_{Se}-$Fe_3Se_{4-x}S_x$/$FeSe_{2-x}S_x$@NSC@rGO are 552.2, 496.9, 479.4, 458.3, 428.6 and 377.5 mA h g^{-1}, respectively, while when the current density is restored to 0.1 A/g, the average discharge capacity can be restored to

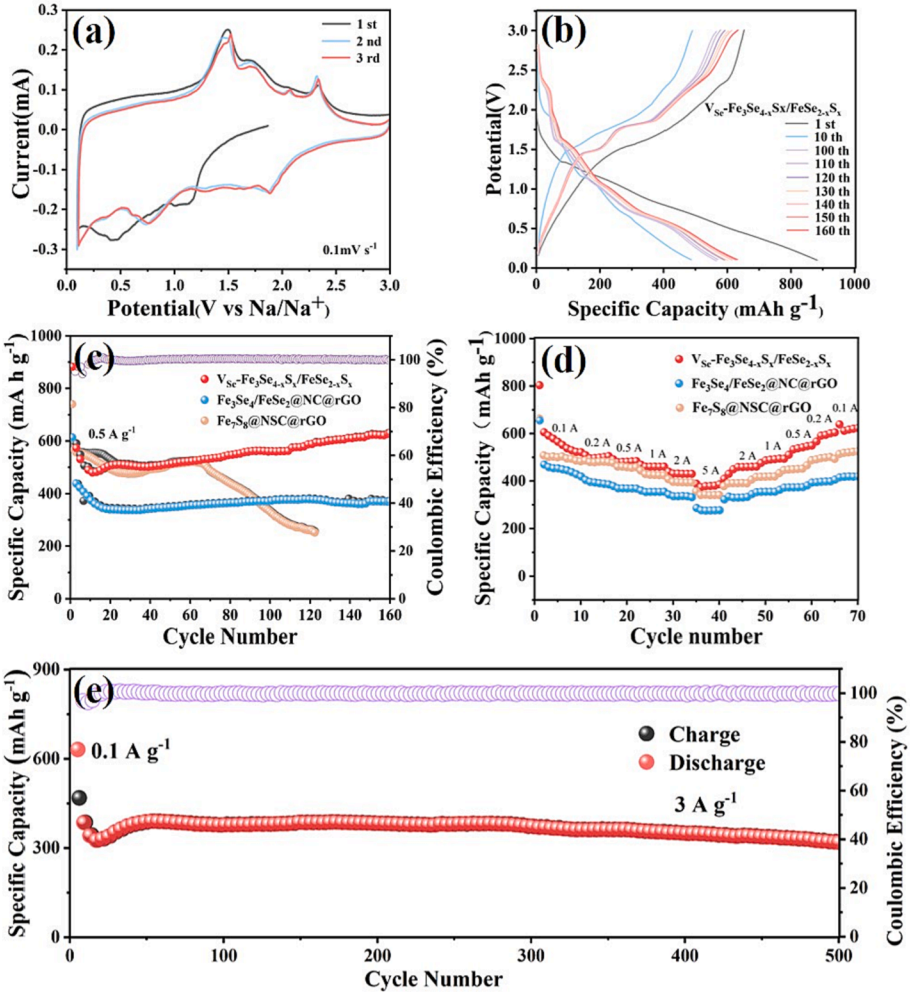

Fig. 5. (a) CV tests of V_{Se}-$Fe_3Se_{4-x}S_x$/$FeSe_{2-x}S_x$@NSC@rGO electrode; (b) Discharge-charge cycle curves at 0.5 A/g; (c) Cycling stability of V_{Se}-$Fe_3Se_{4-x}S_x$/$FeSe_{2-x}S_x$@NSC@rGO, Fe_3Se_4/$FeSe_2$@NC@rGO and Fe_7S_8@NSC@rGO cathodes at 0.5 A/g; (d) Rate performance of V_{Se}-$Fe_3Se_{4-x}S_x$/$FeSe_{2-x}S_x$@NSC@rGO, Fe_3Se_4/$FeSe_2$@NC@rGO and Fe_7S_8@NSC@rGO; (e) Long-term cyclic stability of V_{Se}-$Fe_3Se_{4-x}S_x$/$FeSe_{2-x}S_x$@NSC@rGO at 3 A/g.

615.4 mA h g^{-1}. The long-cycle test in Fig. 5e further indicates that the V_{Se}-$Fe_3Se_{4-x}S_x$/$FeSe_{2-x}S_x$@NSC@rGO electrode is one of the promising candidates as long-life anodes for SIBs. After 500 cycles, the V_{Se}-$Fe_3Se_{4-x}S_x$/$FeSe_{2-x}S_x$@NSC@rGO electrode retains 319.8 mA h g^{-1} at 3 A/g (79.9 % capacity retention and 0.016 % capacity decay per cycle). As shown in Fig. S7 (a-c), the V_{Se}-$Fe_3Se_{4-x}S_x$/$FeSe_{2-x}S_x$@NSC@rGO electrode do not fall off and chap after 50 and 100 cycles at 0.5 A/g compared with that before cycling. And the V_{Se}-$Fe_3Se_{4-x}S_x$/$FeSe_{2-x}S_x$@NSC@rGO composite presented in Fig. S7 (e-f) still maintains the 3D cross-linked structure, being consistent with that before cycling, indicating that the double carbon confinement strategy can effectively alleviate the volume change, pulverization and agglomeration of the material during cycling. In addition, according to previous studies [50,51], Cu element in the electrode may penetrate into the active material of the electrode during cycling, further improving the sodium storage performance of the material. As shown in Fig. S8 and Tab. S2, Cu element is detected in the electrode material after 300 cycles and the molar ratio of Cu to Fe element is 1:7.7. In order to make the sodium storage performance of the V_{Se}-$Fe_3Se_{4-x}S_x$/$FeSe_{2-x}S_x$@NSC@rGO composite more comparable, the cycling performance of the rGO is tested at 0.5 A/g and 3 A/g. Fig. S9 (a-b) shows that the rGO has a capacity of 161.8 mA h g^{-1} after 100 cycles at 0.5 A/g and 111.8 mA h g^{-1} after 500 cycles at 3 A/g, respectively. In order to verify the practicability of the V_{Se}-$Fe_3Se_{4-x}S_x$/$FeSe_{2-x}S_x$@NSC@rGO anode material, the full battery is assembled using the V_{Se}-$Fe_3Se_{4-x}S_x$/$FeSe_{2-x}S_x$@NSC@rGO as the anode, the $Na_3V_2(PO4)_3$ as the cathode, and the $NaPF_6$ non-aqueous solution (NP-005) as the electrolyte. Fig S10a shows the simulation diagram of the full battery. From Fig. S10b, the V_{Se}-$Fe_3Se_{4-x}S_x$/$FeSe_{2-x}S_x$@NSC@rGO//$Na_3V_2(PO_4)_3$ contributes a reversible capacity of 59.6 mA h g^{-1} after 100 cycles at 0.5 A/g, suggesting that the V_{Se}-$Fe_3Se_{4-x}S_x$/$FeSe_{2-x}S_x$@NSC@rGO anode material has a certain practical application prospect.

To further explore the rationales for the excellent performance of the V_{Se}-$Fe_3Se_{4-x}S_x$/$FeSe_{2-x}S_x$@NSC@rGO as an advanced anode material for SIBs, CV curves test at various scan rates, electrochemical impedance spectroscopy (EIS) analysis and galvanostatic intermittent titration technique (GITT) test are performed. As shown in Fig. 6a, at the scanning rates of 0.2 – 1.0 mV s^{-1}, the CV curves exhibits similar profile accompanied by small peak displacement along with the increasing scanning rate, indicating that the V_{Se}-$Fe_3Se_{4-x}S_x$/$FeSe_{2-x}S_x$@NSC@rGO electrode has slight polarization and excellent reversibility [16]. Based on previous studies [52–54], the charge storage is controlled by both ionic diffusion contribution and pseudo-capacitance contribution. The contribution ratio of the pseudo-capacitance can be determined quantitatively by the following equations:

$$i_1 = av^b \tag{1}$$

$$\log(i_1) = b\log(v) + \log(a) \tag{2}$$

where, i_1 and v represent peak current and scan rate, respectively, and a

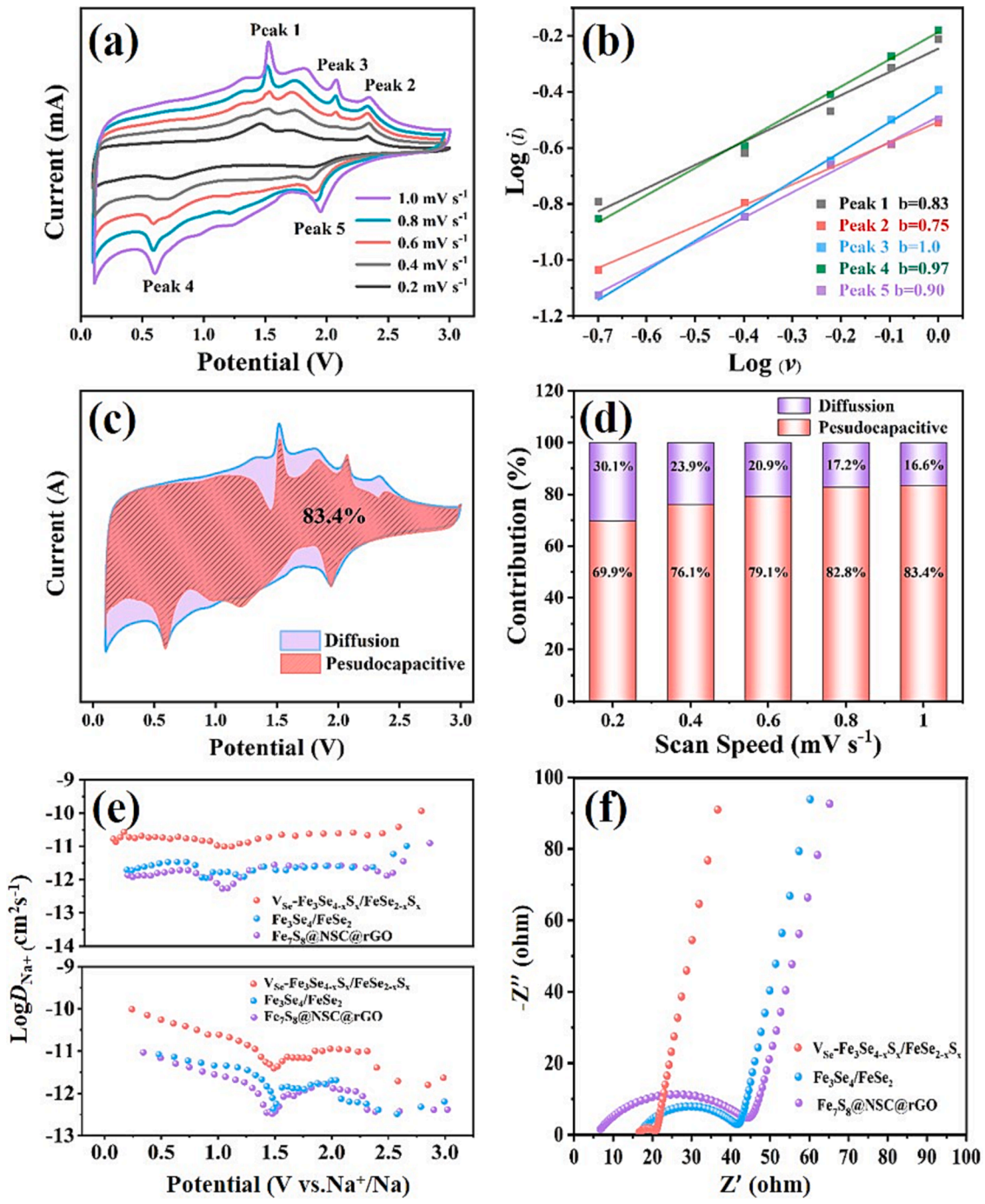

Fig. 6. (a) CV curves of V_{Se}-$Fe_3Se_{4-x}S_x$/$FeSe_{2-x}S_x$@NSC@rGO at different scan rates from 0.2 to 1.0 mV s^{-1}; (b) Fitting lines of log *v* (scan rate)-log *i* (peak current) for V_{Se}-$Fe_3Se_{4-x}S_x$/$FeSe_{2-x}S_x$@NSC@rGO; (c) Contribution of the pseudo-capacitance (the red area) to the total capacity at a scan rate of 1.0 mV s^{-1}; (d) Bar chart of ratio of pseudo-capacitance to total capacity at different scan rates; (e) Calculated log(D_{Na+}) of the three samples; (f) Nyquist plot of V_{Se}-$Fe_3Se_{4-x}S_x$/$FeSe_{2-x}S_x$@NSC@rGO-based battery, Fe_3Se_4/$FeSe_2$@NC@rGO-based battery and Fe_7S_8@NSC@rGO-based battery. (For interpretation of the references to colour in this figure legend, the reader is referred to the web version of this article.)

and b are adjustable parameters. In general, when the b value is close to 0.5, the process is controlled by ion diffusion, while when the b value is close to 1, the capacitive control process is dominant [55]. As shown in Fig. 6b, the anode peak fitting b values are 0.83, 0.75 and 1.0, respectively, while the cathode peak fitting b values are 0.97 and 0.90, respectively. Clearly, Na^+ storage in the electrode is mainly controlled by the pseudo-capacitance behavior [56]. Furthermore, the specific proportion of the contribution of pseudo-capacitance to the total capacity can be calculated from Equation (3):

$$i = k_1 v + k_2 v^{1/2} \quad (3)$$

The former $k_1 v$ represents the contribution of the pseudo-capacitance process to the total current value (*i*), and the latter $k_2 v^{1/2}$ represents the contribution of the diffusion process to the total current. According to the calculation, as shown in Fig. 6c, when the scan rate is 1.0 mV s^{-1}, the contribution of the pseudo-capacitance accounts for 83.4 % of the total charge. At scan rates of 0.2 mV s^{-1} to 1.0 mV s^{-1}, the contribution of the pseudo-capacitor increases from 69.9 % to 83.4 % (Fig. 6d). The

high contribution of pseudo-capacitors to the total capacity is attributed to the existence of a large number of Se vacancies that can expose more active sites and provide three-dimensional transport paths for Na^+, thus enhancing the electrochemical reaction kinetics of the materials.

The diffusion coefficient of Na^+ is measured by GITT at the voltage range of 0.1 V – 3.0 V. The diffusion coefficient of Na^+ can be obtained by Equation (4):

$$D_{Na+} = (4/\pi\tau)\hat{A}\cdot(n_m\hat{A}\cdot V_m/S)^2\hat{A}\cdot(\Delta Es/\Delta Et)^2 \quad (4)$$

where t, n_m, V_m, S, ΔEs and ΔEt represent the intermittent time, molar mass, molar volume, electrode cross-sectional area, voltage change caused by pulse and constant current, respectively [46]. As shown in Fig. 6e, the Na^+ diffusion coefficient of the V_{Se}-$Fe_3Se_{4-x}S_x$/$FeSe_{2-x}S_x$@NSC@rGO electrode is higher than those of Fe_3Se_4/$FeSe_2$@NC@rGO and Fe_7S_8@NSC@rGO electrodes in the processes of charge and discharge.

The Nyquist diagram consists of the arched part of the high-frequency region and the linear part of the low-frequency region (Fig. 6f). By equivalent circuit analysis (Fig. S11), R_e, R_f and R_{ct} are electrolyte resistance, electrode surface film resistance and charge transfer resistance, respectively. As shown in Fig. 6f, the initial R_{ct} (4.1 Ω) of the V_{Se}-$Fe_3Se_{4-x}S_x$/$FeSe_{2-x}S_x$@NSC@rGO electrode is much smaller than those of the Fe_3Se_4/$FeSe_2$@NC@rGO (24.8 Ω) and Fe_7S_8@NSC@rGO (37.6 Ω) electrodes. The results show that the introduction of heteroatoms and the formation of Se vacancies significantly improve the charge transfer kinetics [39].

According to CV test curve and previous reports [52,57–59], the sodium storage mechanism of V_{Se}-$Fe_3Se_{4-x}S_x$/$FeSe_{2-x}S_x$@NSC@rGO is inferred as follows:

$$Fe_3Se_{4-x}S_x + x\ Na^+ + x\ e^- \leftrightarrow Na_xFe_3Se_{4-x}S_x \quad (5)$$

$$FeSe_{2-x}S_x + x\ Na^+ + x\ e^- \leftrightarrow Na_xFeSe_{2-x}S_x \quad (6)$$

$$Na_xFe_3Se_{4-x}S_x + (8\text{-}x)\ Na^+ + (8\text{-}x)\ e^- \leftrightarrow Na_{8-2x}Se_{4-x} + Na_{2x}S_x + 3Fe \quad (7)$$

$$Na_xFeSe_{2-x}S_x + (4\text{-}x)\ Na^+ + (4\text{-}x)\ e^- \leftrightarrow Na_{4-2x}Se_{2-x} + Na_{2x}S_x + Fe \quad (8)$$

Here, Equations (5) and (6) represent the Na^+ embedding process, which takes place at 1.75 V – 2 V. Equations (7) and (8) show the conversion reaction during sodium storage, which occurs at about 0.75 V. Since the above sodium storage reactions are all reversible reactions, according to the out-of-situ XRD and CV test curves [60], the reverse reaction process of Equations (7) and (8) occurs at 1.5 V and 1.7 V, respectively, and the Na^+ removal process of Equations (5) and (6)

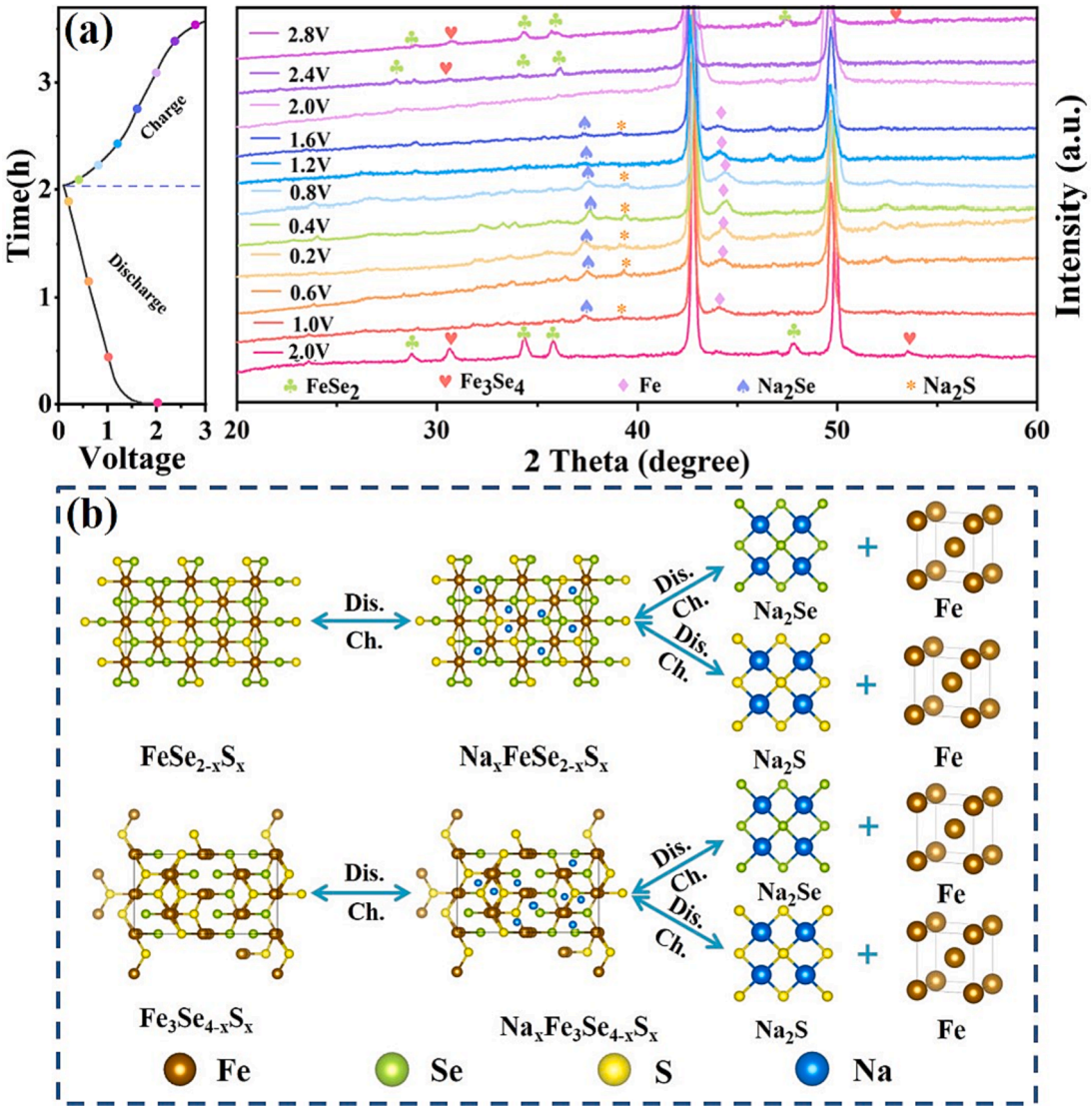

Fig. 7. (a) Charge–discharge curves at 0.5 A/g and matching ex-situ XRD patterns of V_{Se}-$Fe_3Se_{4-x}S_x$/$FeSe_{2-x}S_x$@NSC@rGO electrode between 0.1 and 3.0 V; (b) Evolution diagram of charging and discharging materials of V_{Se}-$Fe_3Se_{4-x}S_x$/$FeSe_{2-x}S_x$@NSC@rGO.

occurs at 2.3 V − 2.4 V.

As shown in Fig. 7a, the galvanostatic charge/discharge (GCD) curve at a current density of 0.5 A/g can be divided into 11 states (OCV; Discharge: 1.0 V, 0.6 V, and 0.2 V; Charge: 0.4 V, 0.8 V, 1.2 V, 1.6 V, 2.0 V, 2.4 V and 2.8 V). It can be seen from Fig. 7a that there are obvious diffraction peaks in the initial state, corresponding to (004) and (−312) crystal planes of Fe_3Se_4 and (101), (111), (012) and (121) crystal planes of $FeSe_2$. During the discharge process, the diffraction peaks of Fe_3Se_4 and $FeSe_2$ gradually disappear, while those of Na_2Se, Na_2S and Fe gradually appear. The presence of Na_2S here proves that the doped S is involved in the process of sodium storage, which is considered to be one of the major reasons for the high capacity of the V_{Se}-$Fe_3Se_{4-x}S_x$/$FeSe_{2-x}S_x$@NSC@rGO. On the contrary, during the charging process, the diffraction peaks of Na_2Se, Na_2S and Fe gradually disappear, while those of Fe_3Se_4 and $FeSe_2$ gradually appear, and finally return to the initial state. The analysis of ex-situ XRD patterns proves our inference on the sodium storage mechanism of the V_{Se}-$Fe_3Se_{4-x}S_x$/$FeSe_{2-x}S_x$@NSC@rGO, which is consistent with Fig. 7b, resulting in good reversibility in the charge and discharge processes.

In order to further explore the synergistic effect of electron density regulation and Se vacancy on Na^+ storage in the material, the first principle calculations (DFT) are performed [61]. Figs. S12(a-d) show the crystal structures of $FeSe_2$, V_{Se}-$FeSe_{2-x}S_x$, Fe_3Se_4 and V_{Se}-$Fe_3Se_{4-x}S_x$, respectively. As expected, Fig. 8(e, f) show that the V_{Se}-$FeSe_{2-x}S_x$ and V_{Se}-$Fe_3Se_{4-x}S_x$ has significantly higher electron state densities at the Fermi level when compared to $FeSe_2$ and Fe_3Se_4 [62,63]. This indicates that the introduction of S regulates the electronic structure, promotes the charge transfer, and improves the intrinsic conductivity of the material. The Climbing-Image NEB method is used to calculate the migration energy barriers of Na^+ in $FeSe_2$, V_{Se}-$FeSe_{2-x}S_x$, Fe_3Se_4 and V_{Se}-$Fe_3Se_{4-x}S_x$ to evaluate the effect of Se vacancy on ion migration [64,65]. The possible migration paths of Na^+ in the four models are shown in Fig. 8(a – d). It is worth noting that the migration energy barriers of Na^+ in the vacancies of the V_{Se}-$FeSe_{2-x}S_x$ and V_{Se}-$Fe_3Se_{4-x}S_x$, as shown in Fig. 8(g, h), are much less than that between the layers of $FeSe_2$ and Fe_3Se_4 [66]. This verifies that the Se vacancy can effectively reduce the diffusion resistance of Na^+ and improve the reaction kinetics of the material. The theoretical calculation results show that the introduction of S leads to the reconstruction of the electronic structure of iron selenide and Se vacancies, which not only improves the conductivity of the material, but also promotes the migration of Na^+ in the electrode material. As a result, the material exhibits excellent sodium storage and rate properties.

4. Conclusion

In summary, we have constructed spatially dual-carbon-confined V_{Se}-$Fe_3Se_{4-x}S_x$/$FeSe_{2-x}S_x$ nanohybrids with abundant Se vacancies by anion doping and carbon confinement engineering. The composite material synthesized by precipitation, freeze-drying and sulfurization/selenization possesses 3D cross-linked structure, alleviating the agglomeration of active substances and achieving excellent cycling performance [67]. In addition, Se vacancy induces the electronic structure transformation of the material and provides a large number of transmission paths for Na^+, promoting the electron transfer and reduces the Na^+ diffusion energy barrier [39]. Therefore, the V_{Se}-$Fe_3Se_{4-x}S_x$/$FeSe_{2-x}S_x$@NSC@rGO has excellent electrochemical performance, giving the reversible capacities of 630.1 mA h g^{-1} after 160 cycles at 0.5 A/g, and 319.8 mA h g^{-1} after 500 cycles at 3 A/g. This study indicates that the excellent structural design and abundant Se vacancies have great potential to improve the storage performance of Na^+ in iron selenides [39,68].

CRediT authorship contribution statement

Peng Wang: Investigation, Methodology, Conceptualization, Writing – original draft, Software. **Yuxiang Chen:** Software, Visualization, Formal analysis. **Xiangyue Liao:** Data curation, Visualization. **Qiaoji Zheng:** Software, Formal analysis. **Ruyi Zhao:** . **Kwok-Ho Lam:** Resources, Validation, Writing – review & editing. **Dunmin Lin:** Resources, Validation, Writing – review & editing, Supervision.

Declaration of competing interest

The authors declare that they have no known competing financial interests or personal relationships that could have appeared to influence the work reported in this paper.

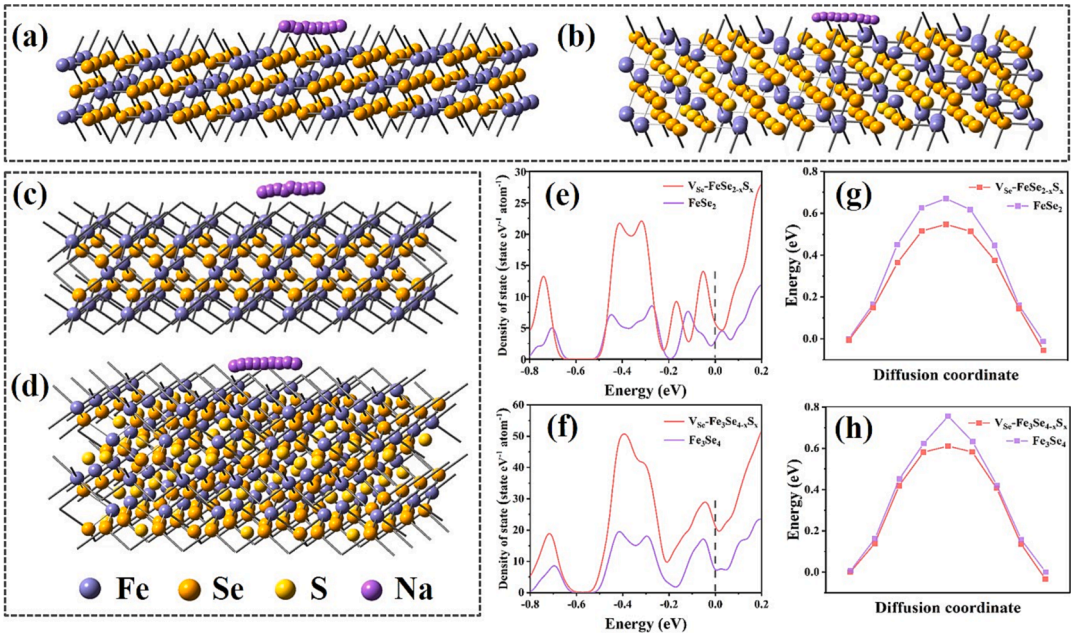

Fig. 8. Schematic representation of Na^+ migration paths in (a) $FeSe_2$, (b) V_{Se}-$FeSe_{2-x}S_x$, (c) Fe_3Se_4 and (d) V_{Se}-$Fe_3Se_{4-x}S_x$; Density of States (DOS) of (e) $FeSe_2$ and V_{Se}-$FeSe_{2-x}S_x$, and (f) Fe_3Se_4 and V_{Se}-$Fe_3Se_{4-x}S_x$; Energy barrier curves of Na^+ diffusion in (g) $FeSe_2$ and V_{Se}-$FeSe_{2-x}S_x$, and (h) Fe_3Se_4 and V_{Se}-$Fe_3Se_{4-x}S_x$.

Data availability

Data will be made available on request.

Acknowledgements

This work was supported by Natural Science Foundation of Sichuan Province (2022NSFSC0222) and Sichuan Science and Technology Program (2023NSFSC0439). The authors also appreciate the Shiyanjia Lab (www.shiyanjia.com) for the SEM tests, eceshi (www.eceshi.cn) for the EPR tests and Beijing Nordson Technology Co., LTD (www.kexingtest.com) for the XPS tests.

Appendix A. Supplementary material

Supplementary data to this article can be found online at https://doi.org/10.1016/j.jcis.2023.11.074.

References

[1] S. Li, K. Wang, G. Zhang, S. Li, Y. Xu, X. Zhang, X. Zhang, S. Zheng, X. Sun, Y. Ma, Fast Charging Anode Materials for Lithium-Ion Batteries: Current Status and Perspectives, Adv. Funct. Mater. 32 (23) (2022) 2200796.
[2] Y. Lu, L. Yu, XW (. D.), Lou,"Nanostructured conversion-type anode materials for advanced lithium-ion batteries," Chem 4(5) (2018) 972-996.
[3] M. Li, J. Lu, z. Chen and K. Amine, Adv. Mater 30 (2018) 1800561.
[4] Y. Zhou, M. Zhang, Q. Han, Y. Liu, Y. Wang, X. Sun, X. Zhang, C. Dong, F. Jiang, Hierarchical 1 T-MoS2/MoOx@ NC microspheres as advanced anode materials for potassium/sodium-ion batteries, Chem. Eng. J. 428 (2022), 131113.
[5] C. Vaalma, D. Buchholz, M. Weil, S. Passerini, The demand for lithium-ion batteries (LIBs) has been increasing since their commer-cialization in 1991 and their widespread use in portable electronics, Nat. Rev. Mater 3 (2018) 18013.
[6] J.-Y. Hwang, S.-T. Myung, Y.-K. Sun, Sodium-ion batteries: present and future, Chem. Soc. Rev. 46 (12) (2017) 3529–3614.
[7] A. Rudola, R. Sayers, C.J. Wright, J. Barker, Opportunities for moderate-range electric vehicles using sustainable sodium-ion batteries, Nat. Energy 8 (3) (2023) 215–218.
[8] R. Huang, Y. Cao, S. Qin, Y. Ren, R. Lan, L. Zhang, Z. Yu, H. Yang, Ultra-high N-doped open hollow carbon nano-cage with excellent Na+ and K+ storage performances, Materials Today Nano 18 (2022), 100217.
[9] M. Yuan, C. Meng, A. Li, B. Cao, Y. Dong, D. Wang, X. Liu, X. Chen, H. Song, A General Multi-Interface Strategy toward Densified Carbon Materials with Enhanced Comprehensive Electrochemical Performance for Li/Na-Ion Batteries, Small 18 (16) (2022) 2105738.
[10] E. Olsson, J. Yu, H. Zhang, H.M. Cheng, Q. Cai, Atomic-Scale Design of Anode Materials for Alkali Metal (Li/Na/K)-Ion Batteries: Progress and Perspectives, Adv. Energy Mater. 12 (25) (2022) 2200662.
[11] J. Wang, X. Yue, Z. Xie, A. Abudula, G. Guan, MOFs-derived transition metal sulfide composites for advanced sodium ion batteries, Energy Storage Mater. 41 (2021) 404–426.
[12] L. Fang, N. Bahlawane, W. Sun, H. Pan, B.B. Xu, M. Yan, Y. Jiang, Conversion-alloying anode materials for sodium ion batteries, Small 17 (37) (2021) 2101137.
[13] T. Tang, G. Ren, Y. Wen, M. Lu, Z. Yao, T. Liu, S. Shen, H. Xie, X. Xia, Y. Yang, Spatially Confined Fe_7S_8 Nanoparticles Anchored on a Porous Nitrogen-Doped Carbon Nanosheet Skeleton for High-Rate and Durable Sodium Storage, ACS Appl. Mater. Interfaces (2023).
[14] C. Li, J. Hou, J. Zhang, X. Li, S. Jiang, G. Zhang, Z. Yao, T. Liu, S. Shen, Z. Liu, Heterostructured NiS_2@ SnS_2 hollow spheres as superior high-rate and durable anodes for sodium-ion batteries, Sci. China Chem. 65 (7) (2022) 1420–1432.
[15] Y. Fang, Z. Chen, L. Xiao, X. Ai, Y. Cao, H. Yang, Recent progress in iron-based electrode materials for grid-scale sodium-ion batteries, Small 14 (9) (2018) 1703116.
[16] J.-S. Park, S.Y. Jeong, K.M. Jeon, Y.C. Kang, J.S. Cho, Iron diselenide combined with hollow graphitic carbon nanospheres as a high-performance anode material for sodium-ion batteries, Chem. Eng. J. 339 (2018) 97–107.
[17] P. Wang, J. Huang, J. Zhang, L. Wang, P. Sun, Y. Yang, Z. Yao, Coupling hierarchical iron cobalt selenide arrays with N-doped carbon as advanced anodes for sodium ion storage, J. Mater. Chem. A 9 (11) (2021) 7248–7256.
[18] F. Zhao, S. Shen, L. Cheng, L. Ma, J. Zhou, H. Ye, N. Han, T. Wu, Y. Li, J. Lu, Improved sodium-ion storage performance of ultrasmall iron selenide nanoparticles, Nano Lett. 17 (7) (2017) 4137–4142.
[19] J. Liu, J. Xie, H. Dong, H. Wei, C. Sun, J. Yang, H. Geng, Iron doping of $NiSe_2$ nanosheets to accelerate reaction kinetics in sodium-ion half/full batteries, Sci. China Mater. 66 (1) (2023) 69–78.
[20] J. Yang, C. Zhang, J. Geng, Y. Sui, H. Wei, C. Sun, H. Geng, Y. Liu, Nickel cobalt selenides on black phosphorene with fast electron transport for high-energy density sodium-ion half/full batteries, Inorg. Chem. Front. 10 (2) (2023) 424–434.
[21] J. Yang, W. Hou, R. Pan, M. Zhou, S. Zhang, Y. Zhang, The interfacial electronic engineering in polyhedral MOF derived Co-doped $NiSe_2$ composite for upgrading rate and longevity performance of aqueous energy storage, J. Alloy. Compd. 897 (2022), 163187.
[22] J. Guo, J. Yang, J. Guan, X. Chen, Y. Zhu, H. Fu, Q. Liu, B. Wei, H. Geng, Interface and electronic structure dual-engineering on $MoSe_2$ with multi-ion/electron transportation channels for boosted sodium-ion half/full batteries, Chem. Eng. J. 450 (2022), 138007.
[23] J. Feng, S.-H. Luo, Y. Zhan, S.-X. Yan, P.-W. Li, L. Zhang, Q. Wang, Y.-H. Zhang, X. Liu, Ingeniously Designed Yolk–Shell-Structured $FeSe_2$@ NDC Nanoboxes as an Excellent Long-Life and High-Rate Anode for Half/Full Na-Ion Batteries, ACS Appl. Mater. Interfaces 13 (43) (2021) 51095–51106.
[24] J. Liu, S. Xiao, X. Li, Z. Li, X. Li, W. Zhang, Y. Xiang, X. Niu, J.S. Chen, Interface engineering of Fe_3Se_4/FeSe heterostructure encapsulated in electrospun carbon nanofibers for fast and robust sodium storage, Chem. Eng. J. 417 (2021), 129279.
[25] Z. Kong, L. Wang, S. Iqbal, B. Zhang, B. Wang, J. Dou, F. Wang, Y. Qian, M. Zhang, L. Xu, Iron Selenide-Based Heterojunction Construction and Defect Engineering for Fast Potassium/Sodium-Ion Storage, Small 18 (15) (2022) 2107252.
[26] D. Sha, Y. You, R. Hu, X. Cao, Y. Wei, H. Zhang, L. Pan, Z. Sun, Comprehensively Understanding the Role of Anion Vacancies on K-Ion Storage: A Case Study of Se-Vacancy-Engineered VSe2, Adv. Mater. 35 (15) (2023) 2211311.
[27] X. Deng, K. Zou, R. Momen, P. Cai, J. Chen, H. Hou, G. Zou, X. Ji, High content anion (S/Se/P) doping assisted by defect engineering with fast charge transfer kinetics for high-performance sodium ion capacitors, Science Bulletin 66 (18) (2021) 1858–1868.
[28] T. Yao, H. Wang, X. Ji, D. Wang, Q. Zhang, L. Meng, J.W. Shi, X. Han, Y. Cheng, Introducing Hybrid Defects of Silicon Doping and Oxygen Vacancies into MOF-Derived TiO2–X@ Carbon Nanotablets Toward High-Performance Sodium-Ion Storage, Small 2302831 (2023).
[29] X. Ma, L. Diao, Y. Wang, Y. Lu, D. Li, D. Yang, X. She, S-vacancies manipulating enhances Na+ insertion of MoS2 for efficient sodium-ion storage, Chem. Eng. J. 457 (2023), 141116.
[30] S. Zhao, Z. Guo, J. Yang, C. Wang, B. Sun, G. Wang, Nanoengineering of Advanced Carbon Materials for Sodium-Ion Batteries, Small 17 (48) (2021) 2007431.
[31] X. Fan, T. Cai, S. Wang, Z. Yang, W. Zhang, Carbon Nanotube-Reinforced Dual Carbon Stress-Buffering for Highly Stable Silicon Anode Material in Lithium-Ion Battery, Small 2300431 (2023).
[32] Z. Pan, X. Zhang, S. Xu, M. Gu, X. Rui, X. Zhang, Chloride-doping, defect and interlayer engineering of copper sulfide for superior sodium-ion batteries, J. Mater. Chem. A 11 (8) (2023) 4102–4110.
[33] H. He, D. Huang, Q. Gan, J. Hao, S. Liu, Z. Wu, W.K. Pang, B. Johannessen, Y. Tang, J.-L. Luo, Anion vacancies regulating endows MoSSe with fast and stable potassium ion storage, ACS Nano 13 (10) (2019) 11843–11852.
[34] J. Liu, L. Zhang, H. Wu, Anion-doping-induced vacancy engineering of cobalt sulfoselenide for boosting electromagnetic wave absorption, Adv. Funct. Mater. 32 (26) (2022) 2200544.
[35] S. Huang, D. Yang, X. Qiu, W. Zhang, Y. Qin, C. Wang, C. Yi, Boosting Surface-Dominated Sodium Storage of Carbon Anode Enabled by Coupling Graphene Nanodomains, Nitrogen-Doping, and Nanoarchitecture Engineering, Adv. Funct. Mater. 32 (33) (2022) 2203279.
[36] S. Yang, S. Wang, D. Chen, W. He, L. Li, Boosting sodium storage performance of Mo_2C via nitrogen-doped carbon sphere encapsulation and rGO wrapping, Chem. Eng. J. 413 (2021), 127471.
[37] M. Wang, B. Qin, S. Wu, Y. Li, C. Liu, Y. Zhang, L. Zeng, H. Fan, Interface ion-exchange strategy of MXene@ $FeIn_2S_4$ hetero-structure for super sodium ion half/full batteries, J. Colloid Interface Sci. 650 (2023) 1457–1465.
[38] R. Sui, G. Zan, M. Wen, W. Li, Z. Liu, Q. Wu, Y. Fu, Dual carbon design strategy for anodes of sodium-ion battery: mesoporous CoS_2/CoO on open framework carbon-spheres with rGO encapsulating, ACS Appl. Mater. Interfaces 14 (24) (2022) 28004–28013.
[39] Y. Xiao, Y. Miao, S. Wan, Y.K. Sun, S. Chen, Synergistic Engineering of Se Vacancies and Heterointerfaces in Zinc-Cobalt Selenide Anode for Highly Efficient Na-Ion Batteries, Small 18 (28) (2022) 2202582.
[40] X. Zhou, X. Yue, Y. Dong, Q. Zheng, D. Lin, X. Du, G. Qu, Enhancing electrochemical performance of electrode material via combining defect and heterojunction engineering for supercapacitors, J. Colloid Interface Sci. 599 (2021) 68–78.
[41] Y.R. Pei, H.Y. Zhou, M. Zhao, J.C. Li, X. Ge, W. Zhang, C.C. Yang, Q. Jiang, High-efficiency sodium storage of Co0. 85Se/WSe2 encapsulated in N-doped carbon polyhedron via vacancy and heterojunction engineering, Carbon, Energy (2023) e374.
[42] Z. Hou, P. Hei, C. Shu, R. Zheng, T. Yang, Q. Zhang, J. Long, Multifunctional Selenium Vacancy Coupling with Interface Engineering Enables High-Stability Li–O_2 Battery, ACS Sustain. Chem. Eng. 8 (17) (2020) 6667–6674.
[43] M. Zhang, L. Zhang, S. Huang, Y. Wang, Y. Si, C. Ma, P. Zhang, Y.-T. Liu, J. Yu, B. Ding, 2D gallium molybdenum selenide grown on a hollow carbon nanofibrous aerogel for high-efficiency electroreduction of nitrogen: Optimized basal plane activity via selenium vacancy modulation, Appl Catal B 292 (2021), 120175.
[44] H. He, H. Zhang, D. Huang, W. Kuang, X. Li, J. Hao, Z. Guo, C. Zhang, Harnessing plasma-assisted doping engineering to stabilize metallic phase MoSe2 for fast and durable sodium-ion storage, Adv. Mater. 34 (15) (2022) 2200397.
[45] Y. Wang, Y. Liu, Q. Li, Z. Li, A. Xu, C. Dong, J. Sun, X. Zhang, X. Sun, J. Yang, New dual-anions $FeS_{0.5}Se_{0.5}$@ NC porous nanorods as advanced electrode materials for wide-temperature sodium-ion half/full batteries, Appl. Surf. Sci. 620 (2023), 156836.
[46] Y. Xiao, Y. Miao, S. Hu, F. Gong, Q. Yu, L. Zhou, S. Chen, Structural Stability Boosted in 3D Carbon-Free Iron Selenide through Engineering Heterointerfaces

with Se-P Bonds for Appealing Na+-Storage, Adv. Funct. Mater. 33 (5) (2023) 2210042.
[47] Q. Liu, R. Xu, D. Mu, G. Tan, H. Gao, N. Li, R. Chen, F. Wu, Progress in electrolyte and interface of hard carbon and graphite anode for sodium-ion battery, Carbon Energy 4 (3) (2022) 458–479.
[48] R. Bi, C. Zeng, H. Huang, X. Wang, L. Zhang, Metal–organic frameworks derived hollow NiS_2 spheres encased in graphene layers for enhanced sodium-ion storage, J. Mater. Chem. A 6 (29) (2018) 14077–14082.
[49] Y. Rao, J. Wang, P. Liang, H. Zheng, M. Wu, J. Chen, F. Shi, K. Yan, J. Liu, K. Bian, Heterostructured WS_2/MoS_2@ carbon hollow microspheres anchored on graphene for high-performance Li/Na storage, Chem. Eng. J. 443 (2022), 136080.
[50] Q. Li, Q. Wei, Q. An, L. Huang, W. Luo, X. Ren, K.A. Owusu, F. Dong, L. Li, P. Zhou, Uncovering the Cu-driven electrochemical mechanism of transition metal chalcogenides based electrodes, Energy Storage Mater. 16 (2019) 625–631.
[51] X. Xu, Y. Liu, X. Luo, G. Ma, F. Tian, Y. Li, D. Zhang, J. Yang, Revisit sodium-storage mechanism of metal selenides in ether-based electrolytes: Electrochemically-driven Cu permeation to the formation of $Cu_{2-x}Se$, Energy Storage Mater. 40 (2021) 189–196.
[52] Q. Li, R. Deng, Y. Chen, J. Gong, P. Wang, Q. Zheng, Y. Huo, F. Xie, X. Wei, C. Yang, Homologous Heterostructured NiS/NiS2@ C Hollow Ultrathin Microspheres with Interfacial Electron Redistribution for High-Performance Sodium Storage, Small 2303642 (2023).
[53] J. Wang, J. Cui, Z. Li, D. Zhang, H. Sun, H. Wang, Q. Wang, H. Woo, S. Ramesh, B. Wang, Polysulfide-derived anion heterogeneous interfaces engineering to facilitate high-efficiency sodium ion storage, Chem. Eng. J. 464 (2023), 142764.
[54] Y. Liu, Y. Qing, B. Zhou, L. Wang, B. Pu, X. Zhou, Y. Wang, M. Zhang, J. Bai, Q. Tang, Yolk-Shell Sb@ Void@ Graphdiyne Nanoboxes for High-Rate and Long Cycle Life Sodium-Ion Batteries, ACS Nano 17 (3) (2023) 2431–2439.
[55] S. Xiao, Z. Li, J. Liu, Y. Song, T. Li, Y. Xiang, J.S. Chen, Q. Yan, Se□ C Bonding Promoting Fast and Durable Na+ Storage in Yolk-Shell SnSe2@ Se□ C, Small 16 (41) (2020) 2002486.
[56] J. Feng, S.h. Luo, S.x. Yan, Y. Zhan, Q. Wang, Y.h. Zhang, X. Liu, L.j. Chang, Rational Design of Yolk-Shell Zn□ Co□ Se@ N-Doped Dual Carbon Architectures as Long-Life and High-Rate Anodes for Half/Full Na-Ion Batteries, Small 17 (46) (2021) 2101887.
[57] M. Xu, Y. Ma, R. Liu, H. Xiao, L. Chen, Z. Zhang, L. Wang, G. Yuan, Constructing electron transport channels in FeSe2 microspheres by a facile strategy for superior long-life and ultrafast sodium-ion storage, Chem. Eng. J. 467 (2023), 143382.
[58] Y. Li, R. Zhang, J. Qian, Y. Gong, H. Li, C. Wu, Y. Bai, F. Wu, Construct NiSe/NiO Heterostructures on NiSe Anode to Induce Fast Kinetics for Sodium-Ion Batteries, Energy Material Advances 4 (2023) 0044.
[59] D. Yan, S. Xiao, X. Li, J. Jiang, Q. He, H. Li, J. Qin, R. Wu, X. Niu, J.S. Chen, NiS_2/FeS Heterostructured Nanoflowers for High-Performance Sodium Storage, Energy Mater. Adv. 4 (2023) 0012.
[60] Y. Li, F. Wu, J. Qian, M. Zhang, Y. Yuan, Y. Bai, C. Wu, Metal chalcogenides with heterostructures for high-performance rechargeable batteries, Small Sci. 1 (9) (2021) 2100012.
[61] P. Giannozzi, S. Baroni, N. Bonini, M. Calandra, R. Car, C. Cavazzoni, D. Ceresoli, G.L. Chiarotti, M. Cococcioni, I. Dabo, QUANTUM ESPRESSO: a modular and open-source software project for quantum simulations of materials, J. Phys. Condens. Matter 21 (39) (2009), 395502.
[62] B. Yu, Y. Ji, X. Hu, Y. Liu, J. Yuan, S. Lei, G. Zhong, Z. Weng, H. Zhan, Z. Wen, Heterostructured Cu_2S@ ZnS/C composite with fast interfacial reaction kinetics for high-performance 3D-printed Sodium-Ion batteries, Chem. Eng. J. 430 (2022), 132993.
[63] C. Zhang, F. Han, F. Wang, Q. Liu, D. Zhou, F. Zhang, S. Xu, C. Fan, X. Li, J. Liu, Improving compactness and reaction kinetics of MoS_2@ C anodes by introducing Fe_9S_{10} core for superior volumetric sodium/potassium storage, Energy Storage Mater. 24 (2020) 208–219.
[64] F. Li, J. Zou, L. Cao, Z. Li, S. Gu, Y. Liu, J. Zhang, H. Liu, Z. Lu, In situ study of K+ electrochemical intercalating into MoS2 flakes, J. Phys. Chem. C 123 (8) (2019) 5067–5072.
[65] Y. Li, K. Chang, E. Shangguan, D. Guo, W. Zhou, Y. Hou, H. Tang, B. Li, Z. Chang, Powder exfoliated MoS_2 nanosheets with highly monolayer-rich structures as high-performance lithium-/sodium-ion-battery electrodes, Nanoscale 11 (4) (2019) 1887–1900.
[66] D. Sha, Y. You, R. Hu, X. Cao, Y. Wei, H. Zhang, L. Pan, Z. Sun, Comprehensively Understanding the Role of Anion Vacancies on K-Ion Storage: A Case Study of Se Vacancy Engineered VSe_2, Advanced materials (Deerfield Beach, Fla.) e2211311.
[67] Z. Sun, X. Wu, Z. Gu, P. Han, B. Zhao, D. Qu, L. Gao, Z. Liu, D. Han, L. Niu, Rationally designed nitrogen-doped yolk-shell Fe_7Se_8/Carbon nanoboxes with enhanced sodium storage in half/full cells, Carbon 166 (2020) 175–182.
[68] K. Qian, L. Li, D. Yang, B. Wang, H. Wang, G. Yuan, J. Bai, S. Ma, G. Wang, Metal-Electronegativity-Induced, Synchronously Formed Hetero-and Vacancy-Structures of Selenide Molybdenum for Non-Aqueous Sodium-Based Dual-Ion Storage, Adv. Funct. Mater. 33 (14) (2023) 2213009.